CONDENSED MATTER PHYSICS

Monolayer 1T-$NbSe_2$ as a 2D-correlated magnetic insulator

Mengke Liu[1], Joshua Leveillee[1,2], Shuangzan Lu[3], Jia Yu[1], Hyunsue Kim[1], Cheng Tian[4], Youguo Shi[4], Keji Lai[1], Chendong Zhang[3], Feliciano Giustino[1,2], Chih-Kang Shih[1]*

Monolayer group V transition metal dichalcogenides in their 1T phase have recently emerged as a platform to investigate rich phases of matter, such as spin liquid and ferromagnetism, resulting from strong electron correlations. Newly emerging 1T-$NbSe_2$ has inspired theoretical investigations predicting collective phenomena such as charge transfer gap and ferromagnetism in two dimensions; however, the experimental evidence is still lacking. Here, by controlling the molecular beam epitaxy growth parameters, we demonstrate the successful growth of high-quality single-phase 1T-$NbSe_2$. By combining scanning tunneling microscopy/spectroscopy and ab initio calculations, we show that this system is a charge transfer insulator with the upper Hubbard band located above the valence band maximum. To demonstrate the electron correlation resulted magnetic property, we create a vertical 1T/2H $NbSe_2$ heterostructure, and we find unambiguous evidence of exchange interactions between the localized magnetic moments in 1T phase and the metallic/superconducting phase exemplified by Kondo resonances and Yu-Shiba-Rusinov–like bound states.

INTRODUCTION

Strong electron correlations underpin many unique phases of quantum matter, including unconventional superconductivity (*1*, *2*), correlated insulator (*3*–*6*), magnetism (*3*, *7*), spin liquids (*8*), and Wigner crystals (*6*, *9*, *10*). Recently, 1T phase group V transition metal dichalcogenides (TMDs) (MX2, with M = V, Nb, Ta; and X = S, Se) have emerged as an interesting platform to explore the rich quantum phases driven by strong electron correlations (*11*–*16*), in particular, Mott insulating state (*17*), charge density wave (CDW) (*18*–*21*), and magnetism (*22*–*25*), especially in the monolayer regime where electron screening is reduced. Among these exotic quantum phases, several outstanding questions remain; for example, (i) whether the insulating gap character is of Mott-Hubbard gap or charge transfer gap needs to be clarified; (ii) the associated magnetic property remain either under heavy debate, such as the ferromagnetism in 1T-VSe_2 (*23*–*25*), or not experimentally verified, such as the quantum spin liquid state in 1T-TaS_2 (*22*).

Newly emerging is the 1T phase $NbSe_2$ that does not occur naturally in bulk crystals (*26*), but it was found that monolayer 1T-$NbSe_2$ can exist during molecular beam epitaxy (MBE) growth on graphene substrate (*27*). This discovery has stimulated many theoretical interests to explore whether correlated electronic phenomena exist in this phase. The calculations revealed that the correlation gap is of charge transfer nature (*28*–*30*), contrary to the previous assumed Mott-Hubbard gap (*27*, *31*). Moreover, it is revealed that the interplay of a CDW and strong electron correlation could lead to the existence of ferromagnetism in monolayer 1T-$NbSe_2$ (*28*, *29*). These prior predictions make monolayer 1T-$NbSe_2$ a unique platform to explore correlation-driven magnetic insulating states.

Here, we report the controlled growth of pure 1T-$NbSe_2$, pure 1H-$NbSe_2$, and their mixed phases in the monolayer regime by fine-tuning the MBE parameters. We probe the electronic structure of monolayer 1T-$NbSe_2$ using scanning tunneling microscopy/spectroscopy (STM/STS). By combining our spectroscopic data with Hubbard-corrected density functional theory (DFT) calculations, we show that the gap is of charge transfer nature. The localized upper Hubbard band (UHB) is located above the valence band maximum (VBM) and the lower Hubbard band (LHB) is found to merge with the valence band. Detailed orbital textures as a function of energy are mapped out and compare favorably with our theoretical calculations, demonstrating the energy-dependent spatial wave function distribution, especially the localization of UHB. We also find that the localized Hubbard band can be easily destroyed by point defects, indicating the fragility of UHB under disorder. To probe the magnetic states in 1T-$NbSe_2$, we create a vertical heterostructure composed of monolayer 1T-$NbSe_2$ on top of metallic/superconducting 2H-$NbSe_2$. Our STS measurements on this heterostructure reveal Kondo resonances (*32*, *33*) and Yu-Shiba-Rusinov (YSR)–like bound states (*34*–*37*), which are clear fingerprints of the exchange interaction between localized magnetic moments in 1T-$NbSe_2$ and the electrons/Cooper pairs in 2H-$NbSe_2$. In addition, the spatial modulation of Kondo peak amplitude correlates with the calculated spin density across the David star CDW, thus providing direct and unambiguous evidence for the existence of large localized magnetic moments driven by electron correlations.

RESULTS

MBE growth and electronic structure of monolayer 1T-$NbSe_2$

Bulk $NbSe_2$ does not occur naturally in the 1T polymorph. Using MBE, we can achieve controlled growth of the 1T and 1H polymorphs of monolayer $NbSe_2$ (Fig. 1, A and B) on both graphite and graphene substrates by changing the growth temperature and the Se-to-Nb flux ratio. Figure 1C shows the parameter space used to control the growth of monolayer $NbSe_2$ on highly oriented pyrolytic graphite (HOPG) substrates. Note that in this parameter space, the

[1]Department of Physics, The University of Texas at Austin, Austin, TX 78712, USA. [2]Oden Institute for Computational Engineering and Sciences, The University of Texas at Austin, Austin, TX 78712, USA. [3]School of Physics and Technology and Key Laboratory of Artificial Micro- and Nano-structures of Ministry of Education, Wuhan University, Wuhan 430027, China. [4]Beijing National Laboratory for Condensed Matter Physics and Institute of Physics, Chinese Academy of Sciences, Beijing 100190, China.
*Corresponding author. Email: shih@physics.utexas.edu

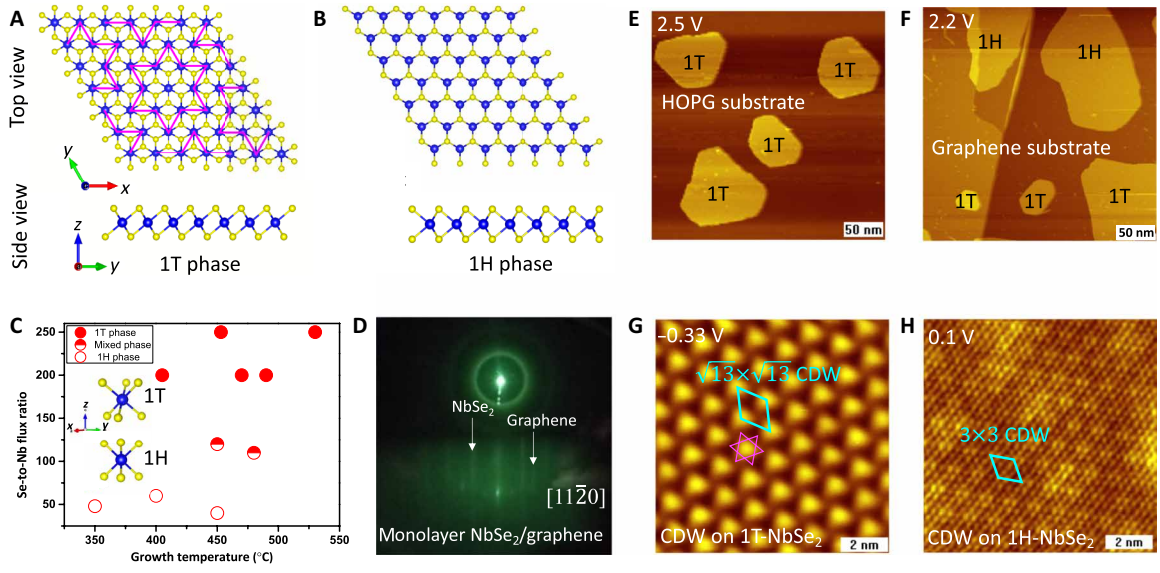

Fig. 1. Growth parameter and structural characterization of monolayer $NbSe_2$. (**A** and **B**) Schematic illustrations of 1T and 2H polymorphs of monolayer $NbSe_2$. The Nb (Se) atoms are shown in blue (yellow). The magenta lines in (A) outline the $\sqrt{13} \times \sqrt{13}$ David star CDW in the 1T phase. (**C**) Growth parameter space for 1T and 1H $NbSe_2$ as a function of growth temperature and the Se-to-Nb flux ratio. Se-to-Nb flux ratio is varied under constant Se vapor pressure. (**D**) The reflection high-energy electron diffraction pattern of monolayer $NbSe_2$ on bilayer graphene/SiC substrate. (**E** and **F**) Large-scale topographic images of $NbSe_2$ flakes. (E) Single 1T phase on HOPG substrate. (F) Coexisting 1T and 1H phases on graphene substrate. (**G** and **H**) STM images of 1T-$NbSe_2$ and 1H-$NbSe_2$. The $\sqrt{13} \times \sqrt{13}$ David star CDW unit cell is marked in (G); the 3×3 CDW unit cell is marked in (H).

same Se deposition rate is kept, while the Nb deposition rate varies. Thus, a high Se-to-Nb flux ratio can also be interpreted as a low growth rate. Under this condition, the pure 1T phase is achieved with a high Se-to-Nb flux ratio over a reasonable range of growth temperature. A reflection high-energy electron diffraction pattern taken on monolayer $NbSe_2$ on a bilayer graphene substrate (Fig. 1D) shows the good crystallinity of our sample. While pure 1T-$NbSe_2$ can be obtained on a graphite substrate, as shown in Fig. 1E and fig. S1A, the same parameters lead to mixed 1H and 1T phases when using epitaxial graphene substrates [graphene-terminated 6H-SiC (0001) substrates] (Fig. 1F), implying that the parameter space for the growth of 1T-$NbSe_2$ on graphene or graphite differs. Additional discussions on MBE growth results can be found in fig. S1.

1T and 1H phase can be distinguished by their CDW periodicities. A $\sqrt{13} \times \sqrt{13}$ CDW is observed on 1T-$NbSe_2$ (Fig. 1G) in direct contrast to the 3 × 3 CDW in the 1H phase (Fig. 1H). Our atomic-scale image of 1T-$NbSe_2$ (Fig. 2A) reveals that the rotation angle of the CDW with respect to its crystal lattice is 13.9°. A 1T phase $NbSe_2$ lattice model stacked on top of the STM image (Fig. 2A) demonstrates the David star shape of the CDW in a supercell consisting of 13 Nb atoms. Within the single-particle picture, this system should be metallic because each David star unit cell contains an odd number of electrons with each Nb atom contributing one d electron. However, our dI/dV STS data reveal an insulating ground state (Fig. 2B). In particular, we find a 150-meV gap, and this gap size is extracted by the energy span range where the STS measures a zero value. We clearly resolve an isolated peak in the density of states (DOS) at 170 meV. Several pronounced peaks are also seen below the Fermi level, however, embedded in a broad continuum background rather than isolated. This insulating ground state can be described by the charge transfer insulator scenario (*3*), as schematically illustrated in Fig. 2C. The strong electron correlation opens a charge gap in the original half-filled band. The band pushed above the Fermi level is labeled as UHB, and the one below the Fermi level is labeled as LHB. The LHB is pushed low enough that it hybridizes with the valence band continuum. Note that these observations directly differ from the previous reported 0.4-eV gap in a Mott-Hubbard insulator scenario (*27*).

This interpretation is consistent with our DFT + U calculations. Shown in Fig. 2D is the band structure calculated with U = 2.95 eV. (See fig. S2 for the discussion of U value chosen.) In the calculation, the energy is referenced to the VBM with the UHB and LHB highlighted in red and their spins in opposite directions. The UHB is nearly isolated and flat with a bandwidth of only 25 meV, while the LHB falls within the valence band continuum thus demonstrating the charge transfer character of this system. In addition, a few pronounced spectral peak features seen in the dI/dV spectrum (Fig. 2B) are also captured in the calculated DOS (Fig. 2E). A careful comparison between calculations and experiments allows us to identify the Γ point energy of the UHB and LHB, as indicated in Fig. 2 (B and E). Although the calculated bandgap is slightly larger than in the experiments (by ~0.1 eV), the calculated DOS shows good agreement with the experimental spectrum. The fact that UHB and LHB are spin-polarized and well separated from the Fermi level suggests the existence of a net magnetic moment and potential magnetic order. We will come back to this point in the section "Localized magnetic moment".

Orbital texture mapping of 1T-$NbSe_2$

We further probe the energy-dependent orbital textures to reveal the spatial wave function distribution, especially the localization of UHB, and compare the results with our calculations. We use a constant height mode to map the dI/dV image (Fig. 3, A to F). Previously,

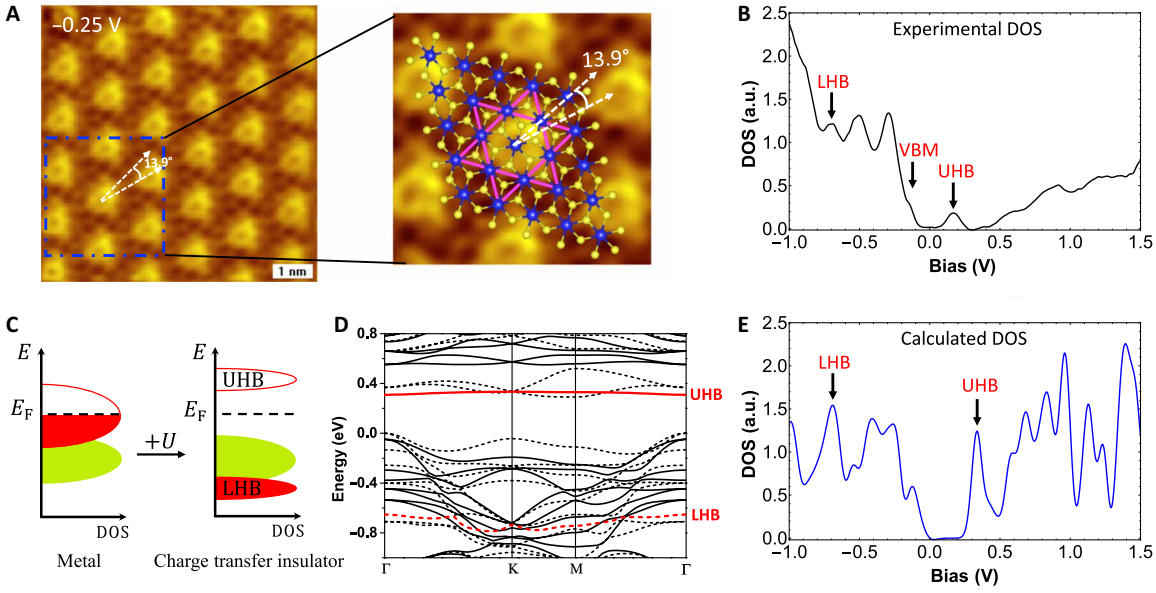

Fig. 2. Charge transfer insulator nature of 1T-$NbSe_2$. (**A**) Atomic-resolution topographic image of 1T-$NbSe_2$. The area enclosed by the blue dashed-dotted square is enlarged with an enhanced color contrast. The 1T-$NbSe_2$ lattice model superimposed on top is aligned with the atomic sites, and the white dashed arrows show the rotation of the CDW relative to the lattice. (**B**) d*I*/d*V* STS spectrum of 1T-$NbSe_2$. The UHB is above the insulating gap and relatively isolated from the conduction band continuum; the LHB is below the VBM and merged with the valence band continuum, as marked by the black arrows. DOS, density of states; a.u., arbitrary units. (**C**) Schematic illustration of energy levels for charge transfer insulator driven by electron correlation *U*. The green band represents the valence band continuum. (**D**) Calculated band structure of 1T-$NbSe_2$ in the $\sqrt{13} \times \sqrt{13}$ CDW ground state. The dashed and solid lines represent up and down spin bands, respectively. The UHB and LHB are highlighted in red. (**E**) Calculated DOS. The black arrows indicate the Γ point energy of UHB and LHB.

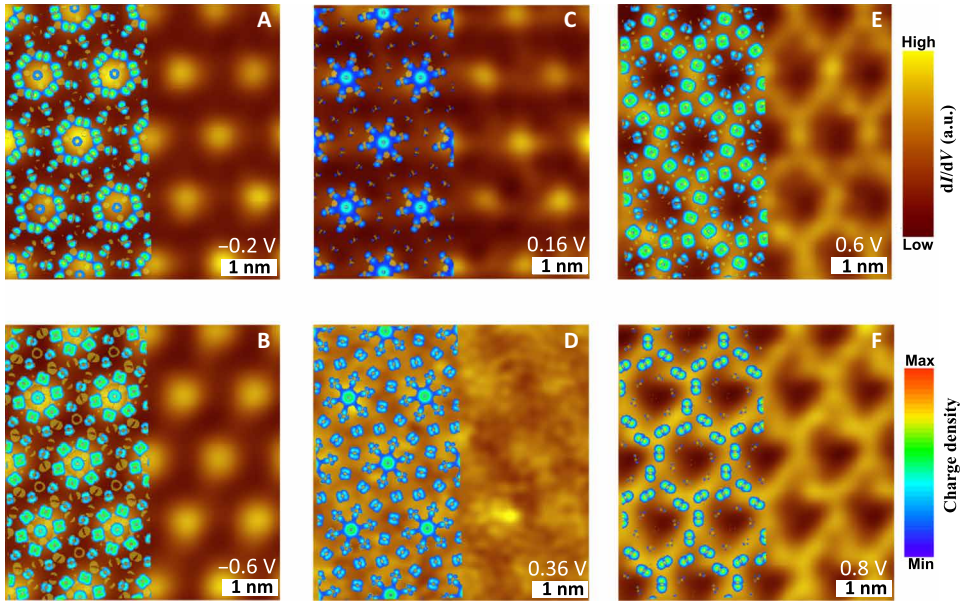

Fig. 3. Orbital texture mapping of 1T-$NbSe_2$. (**A** to **F**) Constant-height d*I*/d*V* images of 1T-$NbSe_2$ at different biases showing energy-dependent orbital textures. The calculated charge density distributions are overlaid on the left half of each d*I*/d*V* image. Extended information on DFT-calculated maximum and minimum charge densities can be found in table S1. Energies at which calculations are performed: (A) E_{VBM} − 0.25 eV; (B) E_{VBM} − 0.65 eV; (C) E_{UHB}; (D) E_{UHB} + 0.25 eV; (E) E_{UHB} + 0.45 eV; (F) E_{UHB} +, 0.7 eV. E_{VBM} and E_{UHB} refer to the energies of VBM and UHB, respectively.

this mode has been shown to reflect the orbital texture better than the constant current d*I*/d*V* image (*38*, *39*) because constant current d*I*/d*V* mode is subjected to a convolution effect due to the modulation of absolute tip-to-sample distance. A detailed comparison and discussion between these two modes can be found in fig. S3. The calculated charge density distribution is superimposed to the STM image (Fig. 3, A to F) and is consistent with the experimental map. Among the valence band, the orbital textures show similar features;

thus, we only show two energies here (Fig. 3 A and B). The d*I*/d*V* images follow the symmetry of the David star CDW with most charge density concentrated on the center of each star (Fig. 3 A and B). A richer orbital texture is found in the conduction band. The orbital texture corresponding to the UHB energy (Fig. 3C) is strongly localized around the central Nb atom. This localization is consistent with the very small bandwidth of the UHB (Fig. 2D). At higher energies, the orbital texture appears to be smeared out (Fig. 3D), and it gradually evolves to become delocalized, forming mesh structures and connecting with other David stars (Fig. 3, E and F), in line with the dispersive nature expected of states in the conduction band continuum. Good agreement in the orbital texture mapping and the theoretical calculation over an extended energy range strongly support the conclusion that the gap is of charge transfer nature, as predicted by the theory. Note that this conclusion differs from a recent report (*31*).

The fragility of UHB at local defect positions

To gain more insight into the properties of the Hubbard band and its localized charge distribution, we investigate the impact of point defects. Shown in Fig. 4A are two defects most commonly observed and naturally formed in 1T-$NbSe_2$. We label these defects as type I and type II on the basis of the morphology of their associated CDW. The type I defect appears as a weakened CDW spot, while the type II defect appears as a missing CDW spot. In direct contrast to the d*I*/d*V* spectra on pristine 1T-$NbSe_2$ (Figs. 4B and 2B), the d*I*/d*V* spectra on type I and type II defects (Fig. 4, C and D) miss the UHB feature. As a result, the insulating gap at these defects' positions is much wider, reaching up to about 0.45 eV. As previously reported, the most commonly formed defects in TMDs are either a metal atom vacancy or a chalcogen atom vacancy (*40*). From the discussion in Figs. 2 and 3, we know that the UHB is strongly localized on the central Nb atom of the David star in pristine 1T-$NbSe_2$; therefore, we hypothesize that a missing David star feature may be associated with a missing central Nb atom. We theoretically choose a Nb atom vacancy model (see fig. S5 for more details) to simulate type II defects. The calculated DOS of this model (Fig. 4E) shows the disappearance of the UHB, consistent with our experimental observation. While a more thorough exploration of point defects in 1T-$NbSe_2$ is warranted, this model confirms the crucial role of the central Nb atom. Putting together the information gathered so far on pristine and defective 1T-$NbSe_2$, we demonstrate the significance of the crystallinity and infer that the David star is crucially linked with the spin-polarized electron density around the central Nb atom and is very sensitive to the local bonding environment.

Localized magnetic moment

Our spin-polarized DFT calculation has a free energy that is 57 meV per David star lower than the spin-nonpolarized case, indicating a magnetic ground state. To explore the localized magnetic moments in 1T-$NbSe_2$, we couple them with an itinerant electron bath by creating 1T-$NbSe_2$/2H-$NbSe_2$ vertical heterostructures following the approach of Bischoff *et al.* (*41*). A schematic illustration is shown in Fig. 5A, and the STM image of the heterostructure is shown in

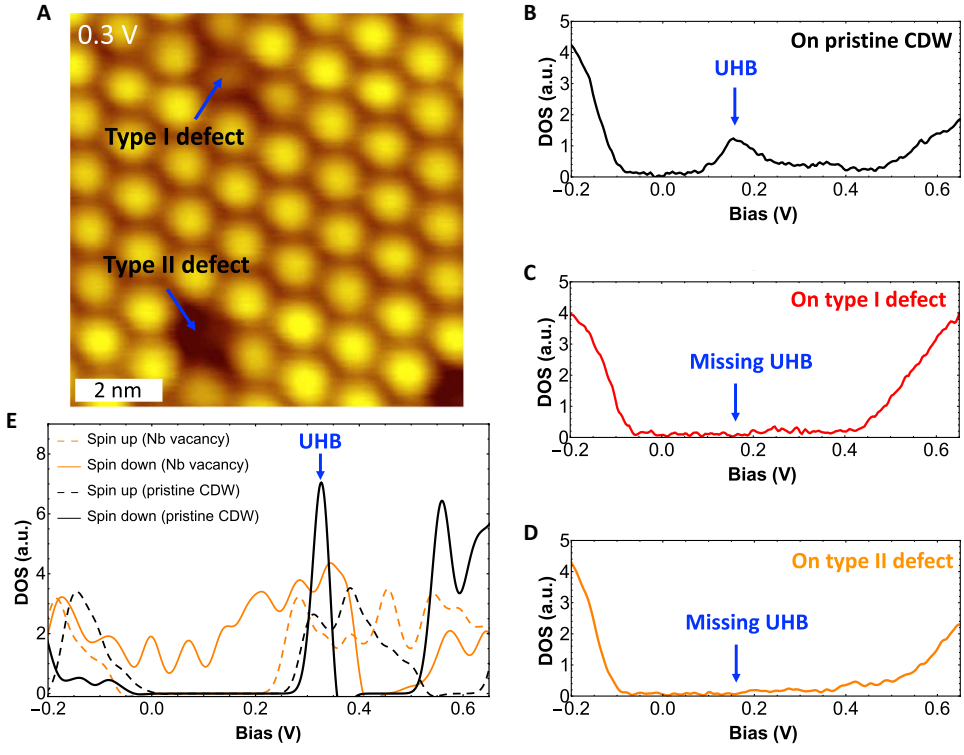

Fig. 4. The fragility of UHB at local defect positions. (**A**) Two types of common defects in 1T-$NbSe_2$. Type I defects label weakened CDW spot. Type II defects label missing CDW spot. (**B** to **D**) Typical d*I*/d*V* spectra taken at pristine CDW and type I and type II defects. In contrast to pristine CDW, d*I*/d*V* spectra on type I and type II defects show missing UHB. (**E**) Calculated DOS for Nb vacancy model (orange lines) and pristine CDW (black lines). The dash and solid lines represent the up and down spin bands, respectively. The spin-polarized UHB appears in the pristine CDW but is missing in the Nb vacancy model.

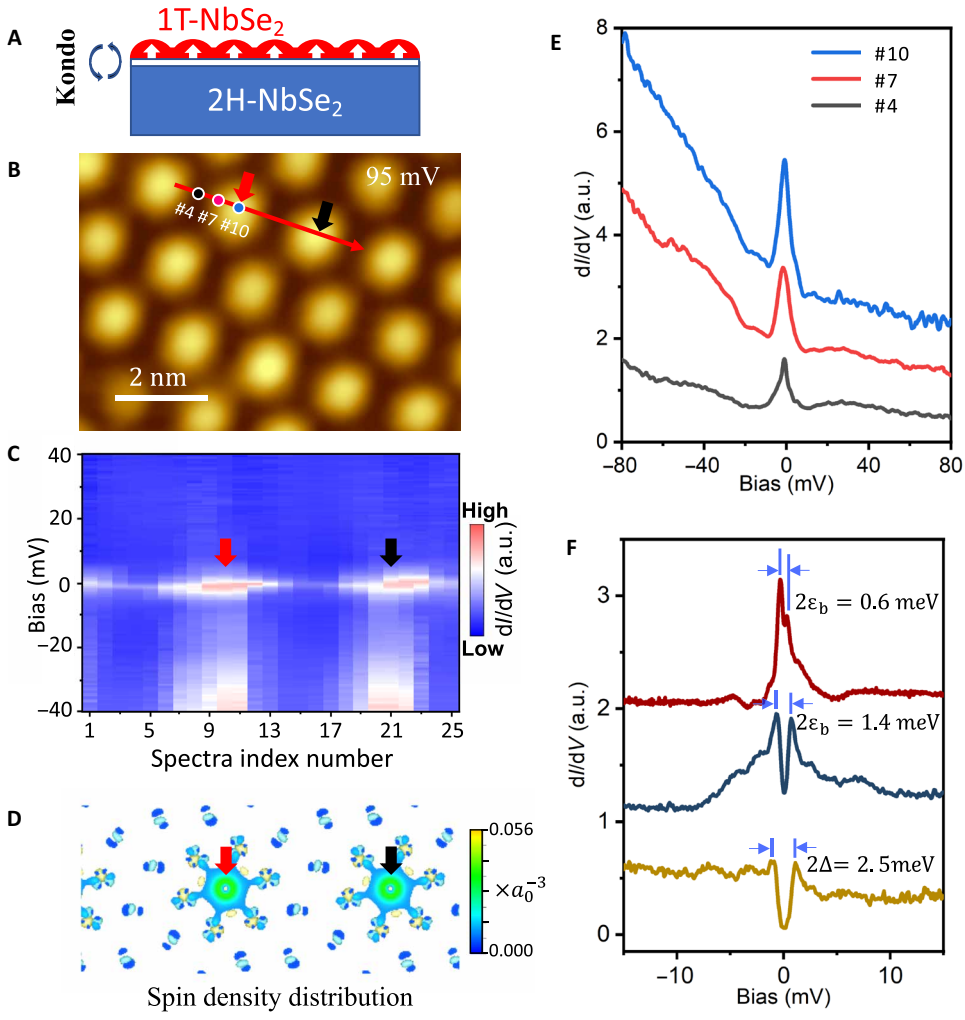

Fig. 5. Localized magnetic moment in 1T-$NbSe_2$. (**A**) Schematics of vertical heterostructure formed by monolayer 1T-$NbSe_2$ on bulk 2H-$NbSe_2$. The height profile in red represents the 1T-$NbSe_2$ CDW. Each unit cell carries a net magnetic moment illustrated by a white arrow, and their directions are artificially set to be parallel. The coupling between the conduction electrons in 2H-$NbSe_2$ and the magnetic moment in 1T-$NbSe_2$ was manifested by the Kondo effect. (**B**) STM image on the heterostructure surface showing the CDW of 1T-$NbSe_2$. (**C**) False-color images of d*I*/d*V* spectra taken along the red line in (B). A periodic modulation of the Kondo peak amplitude was observed, and the two maxima marked by the red and black arrows correspond to the CDW centers. (**D**) Calculated spin density distribution in unit of a_0^{-3}, where a_0 is the Bohr radius. The red and black arrows mark the CDW centers. (**E**) Selected d*I*/d*V* spectra from (C) (index numbers #4, #7, and #10). Their positions are marked in (B) with the corresponding colors. (**F**) d*I*/d*V* spectra with finer energy resolution on the heterostructure surface demonstrate the coexistence of YSR bound state and the Kondo resonance (red and dark blue lines); ε_b labels the binding energy of the YSR states. For comparison, the dark yellow line plots the d*I*/d*V* spectrum taken on pristine bulk 2H-$NbSe_2$, which exhibits superconductivity; Δ labels the superconducting gap.

Fig. 5B. Detailed information of the 1T/2H heterostructure including the formation mechanism can be found in fig. S6. The magnetic moments in the 1T phase, as predicted by our calculations, interact with the electrons near the Fermi surface of the 2H phase that should lead to Kondo resonances. This is what the experiment shows. Figure 5C shows the spatial d*I*/d*V* mapping acquired at 0.35 K, and Fig. 5D shows the corresponding spin density distribution, majority spin minus minority spin, calculated by DFT. The d*I*/d*V* mapping (Fig. 5C) and the selected spectra (Fig. 5E) show clear Kondo resonances; in addition, the spatial modulation of the Kondo resonance peak amplitude (Fig. 5, C and E) correlates very well with the calculated spin density distribution in the 1T phase (Fig. 5D), suggesting a Kondo lattice platform (*42*). These data provide unambiguous evidence that the observed Kondo resonances result from the interaction between Fermi surface electrons in the 2H phase (metal) and the magnetic moment of the David star in the 1T phase (charge transfer insulator).

Because bulk 2H-$NbSe_2$ is also a superconductor with a critical temperature of 7.2 K, the exchange interaction between the magnetic moments in the 1T phase and the Cooper pairs in the 2H phase should also lead to YSR-like bound states below the superconducting critical temperature (*34*–*36*). The spectra shown in Fig. 5 (C and E) are acquired with a lock-in amplifier modulation amplitude of 2.0 meV (peak-to-valley), exceeding the bound state energy separation. With a finer energy resolution (0.1-meV energy step and 0.4-meV lock-in modulation amplitude), the bound states are observed. In

Fig. 5F, we show two representative spectra acquired on the 1T phase, along with the superconducting gap observed on the neighboring 2H phase. In the 1T region, multiple YSR-like bound states appear superimposed to the Kondo resonance background, thus demonstrating the interplay between Kondo physics and superconductivity (*37*, *43*–*45*). Note that the broader Kondo width compared to the bound state binding energy indicates a regime of "spin-screen" (*37*, *46*, *47*), in which Kondo resonance and bound state coexist. Extended discussion can be found in the Supplementary Materials. While the binding energies of these bound states and the electron-hole spectral weight asymmetry depend on the microscopic details of the exchange interaction, Coulomb repulsion, and superconducting pairing (*43*, *48*–*50*) and certainly deserve a separate investigation, our current measurements provide additional strong evidence for the localized magnetic moments in 1T-$NbSe_2$.

DISCUSSION

In this work, we have achieved a controlled growth of monolayer single-phase 1T-$NbSe_2$ on both graphite and bilayer graphene/SiC substrates, and we demonstrated that this new system is a charge transfer insulator. We find a nondispersive UHB associated with the central Nb atom of the David star resulting from the $\sqrt{13} \times \sqrt{13}$ CDW reconstruction, and we show that this feature is very sensitive to the local bonding environment, demonstrating the essential role of crystallinity when revealing its intrinsic property. Further experiments such as in situ atomic force microscopy are needed to address more specific characters of defects. By fabricating insulator/superconductor heterostructures of 1T and 2H $NbSe_2$, we provide direct and unambiguous evidence for localized magnetic moments via the observation of Kondo resonances and YSR-like bound states. Note that the interlayer coupling between the 1T and 2H $NbSe_2$ may alter the inter–David star exchange interaction, and as a result, the long-range magnetic order in the 1T/2H $NbSe_2$ may be different from a suspended monolayer 1T-$NbSe_2$; thus, further investigations are needed to conclude whether long-range magnetic order exists in the monolayer 1T-$NbSe_2$. Having demonstrated the controlled growth and orbital texture mapping of pure phases of 1T-$NbSe_2$ and 2H-$NbSe_2$ as well as their mixed phases and heterostructures, we believe that $NbSe_2$ now offers a uniquely versatile platform to investigate the interplay of charge, spin, and lattice degrees of freedoms in two dimensions, as well as to advance our understanding of magnetism and superconductivity in atomically thin crystals.

MATERIALS AND METHODS

Sample growth and STM/STS measurements

Monolayer 1T-$NbSe_2$ was grown in a home-built MBE chamber with base pressure at~10^{-10} torr. High-purity Nb (99.9%) and high-purity Se (99.999%) were evaporated from an e-beam evaporator and a standard Knudsen cell, respectively. The flux ratio was determined using crystal monitor. Samples were transferred from MBE into STM, base pressure ~10^{-11} torr, through a transfer vessel, base pressure~10^{-10} torr, to maintain the perfect crystallinity of the film. STM/STS measurements were conducted at 4.3 K except for the measurements of Kondo and YSR bound states, which were performed at 0.35 K. The W tip was prepared by an electrochemically etched W tip treated with in situ electron beam cleaning. STM dI/dV spectra were measured using a standard lock-in technique with feedback loop off, whose modulation frequency is 490 Hz. Constant height dI/dV mappings were performed with feedback loop open.

DFT calculations

DFT calculations are performed in the Quantum ESPRESSO software package (*51*). The Perdew-Burke-Ernzerhof (PBE) exchange correlation function is used to approximate the exchange and correlation energy (*52*). Nb and Se scalar relativistic optimally norm-conserving Vanderbilt pseudopotentials from the PseudoDojo repository are used (*53*). On-site correlation on the Nb-4d states is treated by performing DFT + U calculations including spin polarization (*54*). A plane wave energy cutoff of 120 rydberg (Ry), a charge density energy cutoff of 480 Ry, a Γ-centered $4 \times 4 \times 1$ k-point integration grid, and 20 Å of vacuum are used to converge the total energy of the cell. The $\sqrt{13} \times \sqrt{13}$ CDW phase unit cell of 1T-$NbSe_2$ is generated by distorting the Nb atoms toward their respective David star centers and relaxing the forces on each atom to below 1×10^{-7} Ry/bohr. Densities of states, orbital textures, and the spin-charge density are calculated non–self consistently on a $16 \times 16 \times 1$ Gamma-centered k-point integration grid. Gaussian broadening factors of 50 and 25 meV are used in Figs. 2E and 4E, respectively.

SUPPLEMENTARY MATERIALS

Supplementary material for this article is available at https://science.org/doi/10.1126/sciadv.abi6339

REFERENCES AND NOTES

1. E. Dagotto, Correlated electrons in high-temperature superconductors. *Rev. Mod. Phys.* **66**, 763–840 (1994).
2. P. A. Lee, N. Nagaosa, X.-G. Wen, Doping a Mott insulator: Physics of high-temperature superconductivity. *Rev. Mod. Phys.* **78**, 17–85 (2006).
3. M. Imada, A. Fujimori, Y. Tokura, Metal-insulator transitions. *Rev. Mod. Phys.* **70**, 1039–1263 (1998).
4. R. Bistritzer, A. H. MacDonald, Moiré bands in twisted double-layer graphene. *Proc. Natl. Acad. Sci. U.S.A.* **108**, 12233–12237 (2011).
5. Y. Cao, V. Fatemi, A. Demir, S. Fang, S. L. Tomarken, J. Y. Luo, J. D. Sanchez-Yamagishi, K. Watanabe, T. Taniguchi, E. Kaxiras, R. C. Ashoori, P. Jarillo-Herrero, Correlated insulator behaviour at half-filling in magic-angle graphene superlattices. *Nature* **556**, 80–84 (2018).
6. Y. Xu, S. Liu, D. A. Rhodes, K. Watanabe, T. Taniguchi, J. Hone, V. Elser, K. F. Mak, J. Shan, Correlated insulating states at fractional fillings of moiré superlattices. *Nature* **587**, 214–218 (2020).
7. Y. Tang, L. Li, T. Li, Y. Xu, S. Liu, K. Barmak, K. Watanabe, T. Taniguchi, A. H. MacDonald, J. Shan, K. F. Mak, Simulation of Hubbard model physics in WSe2/WS2 moiré superlattices. *Nature* **579**, 353–358 (2020).
8. P. W. Anderson, Resonating valence bonds: A new kind of insulator? *Mater. Res. Bull.* **8**, 153–160 (1973).
9. E. Wigner, On the interaction of electrons in metals. *Phys. Rev.* **46**, 1002–1011 (1934).
10. E. C. Regan, D. Wang, C. Jin, M. I. Bakti Utama, B. Gao, X. Wei, S. Zhao, W. Zhao, Z. Zhang, K. Yumigeta, M. Blei, J. D. Carlström, K. Watanabe, T. Taniguchi, S. Tongay, M. Crommie, A. Zettl, F. Wang, Mott and generalized Wigner crystal states in WSe2 /WS2 moiré superlattices. *Nature* **579**, 359–363 (2020).
11. B. Sipos, A. F. Kusmartseva, A. Akrap, H. Berger, L. Forró, E. Tutiš, From Mott state to superconductivity in 1T-TaS2. *Nat. Mater.* **7**, 960–965 (2008).
12. Y. Yu, F. Yang, X. F. Lu, Y. J. Yan, Y.-H. Cho, L. Ma, X. Niu, S. Kim, Y.-W. Son, D. Feng, S. Li, S.-W. Cheong, X. H. Chen, Y. Zhang, Gate-tunable phase transitions in thin flakes of 1T-TaS2. *Nat. Nanotechnol.* **10**, 270–276 (2015).
13. D. Cho, S. Cheon, K.-S. Kim, S.-H. Lee, Y.-H. Cho, S.-W. Cheong, H. W. Yeom, Nanoscale manipulation of the Mott insulating state coupled to charge order in 1*T*-TaS_2. *Nat. Commun.* **7**, 10453 (2016).
14. S. Qiao, X. Li, N. Wang, W. Ruan, C. Ye, P. Cai, Z. Hao, H. Yao, X. Chen, J. Wu, Y. Wang, Z. Liu, Mottness collapse in 1T-$TaS_{2-x}Se_x$ transition-metal dichalcogenide: An interplay between localized and itinerant orbitals. *Phys. Rev. X* **7**, 041054 (2017).
15. S.-H. Lee, J. S. Goh, D. Cho, Origin of the insulating phase and first-order metal-insulator transition in 1*T*–TaS_2. *Phys. Rev. Lett.* **122**, 106404 (2019).

16. W. Wang, B. Wang, Z. Gao, G. Tang, W. Lei, X. Zheng, H. Li, X. Ming, C. Autieri, Charge density wave instability and pressure-induced superconductivity in bulk 1*T*–NbS_2. *Phys. Rev. B* **102**, 155115 (2020).
17. Y. Chen, W. Ruan, M. Wu, S. Tang, H. Ryu, H.-Z. Tsai, R. Lee, S. Kahn, F. Liou, C. Jia, O. R. Albertini, H. Xiong, T. Jia, Z. Liu, J. A. Sobota, A. Y. Liu, J. E. Moore, Z.-X. Shen, S. G. Louie, S.-K. Mo, M. F. Crommie, Strong correlations and orbital texture in single-layer 1T-$TaSe_2$. *Nat. Phys.* **16**, 218–224 (2020).
18. J. A. Wilson, F. J. Di Salvo, S. Mahajan, Charge-density waves and superlattices in the metallic layered transition metal dichalcogenides. *Adv. Phys.* **24**, 117–201 (1975).
19. M. Chhowalla, H. S. Shin, G. Eda, L.-J. Li, K. P. Loh, H. Zhang, The chemistry of two-dimensional layered transition metal dichalcogenide nanosheets. *Nat. Chem.* **5**, 263–275 (2013).
20. T. Ritschel, J. Trinckauf, K. Koepernik, B. Büchner, M. v. Zimmermann, H. Berger, Y. I. Joe, P. Abbamonte, J. Geck, Orbital textures and charge density waves in transition metal dichalcogenides. *Nat. Phys.* **11**, 328–331 (2015).
21. G. Duvjir, B. K. Choi, I. Jang, S. Ulstrup, S. Kang, T. Thi Ly, S. Kim, Y. H. Choi, C. Jozwiak, A. Bostwick, E. Rotenberg, J.-G. Park, R. Sankar, K.-S. Kim, J. Kim, Y. J. Chang, Emergence of a metal–insulator transition and high-temperature charge-density waves in VSe_2 at the monolayer limit. *Nano Lett.* **18**, 5432–5438 (2018).
22. K. T. Law, P. A. Lee, 1T-TaS_2 as a quantum spin liquid. *Proc. Natl. Acad. Sci. U.S.A.* **114**, 6996–7000 (2017).
23. M. Bonilla, S. Kolekar, Y. Ma, H. C. Diaz, V. Kalappattil, R. Das, T. Eggers, H. R. Gutierrez, M.-H. Phan, M. Batzill, Strong room-temperature ferromagnetism in VSe_2 monolayers on van der Waals substrates. *Nat. Nanotechnol.* **13**, 289–293 (2018).
24. A. O. Fumega, M. Gobbi, P. Dreher, W. Wan, C. González-Orellana, M. Peña-Díaz, C. Rogero, J. Herrero-Martín, P. Gargiani, M. Ilyn, M. M. Ugeda, V. Pardo, S. Blanco-Canosa, Absence of ferromagnetism in VSe_2 caused by its charge density wave phase. *J. Phys. Chem. C* **123**, 27802–27810 (2019).
25. W. Yu, J. Li, T. S. Herng, Z. Wang, X. Zhao, X. Chi, W. Fu, I. Abdelwahab, J. Zhou, J. Dan, Z. Chen, Z. Chen, Z. Li, J. Lu, S. J. Pennycook, Y. P. Feng, J. Ding, K. P. Loh, Chemically exfoliated VSe_2 monolayers with room-temperature ferromagnetism. *Adv. Mater.* **31**, 1903779 (2019).
26. F. Kadijk, F. Jellinek, On the polymorphism of niobium diselenide. *J. Less Common Met.* **23**, 437–441 (1971).
27. Y. Nakata, K. Sugawara, R. Shimizu, Y. Okada, P. Han, T. Hitosugi, K. Ueno, T. Sato, T. Takahashi, Monolayer 1*T*-$NbSe_2$ as a Mott insulator. *NPG Asia Mater.* **8**, e321 (2016).
28. M. Calandra, Phonon-assisted magnetic mott-insulating state in the charge density wave phase of single-layer 1*T*–$NbSe_2$. *Phys. Rev. Lett.* **121**, 026401 (2018).
29. D. Pasquier, O. V. Yazyev, Charge density wave phase, Mottness, and ferromagnetism in monolaye r 1*T*–$NbSe_2$. *Phys. Rev. B* **98**, 045114 (2018).
30. E. Kamil, J. Berges, G. Schönhoff, M. Rösner, M. Schüler, G. Sangiovanni, T. O. Wehling, Electronic structure of single layer 1T-$NbSe_2$: Interplay of lattice distortions, non-local exchange, and Mott–Hubbard correlations. *J. Phys. Condens. Matter* **30**, 325601 (2018).
31. L. Liu, H. Yang, Y. Huang, X. Song, Q. Zhang, Z. Huang, Y. Hou, Y. Chen, Z. Xu, T. Zhang, X. Wu, J. Sun, Y. Huang, F. Zheng, X. Li, Y. Yao, H.-J. Gao, Y. Wang, Direct identification of Mott Hubbard band pattern beyond charge density wave superlattice in monolayer 1T-$NbSe_2$. *Nat. Commun.* **12**, 1978 (2021).
32. J. Kondo, Resistance minimum in dilute magnetic alloys. *Prog. Theor. Phys.* **32**, 37–49 (1964).
33. K. Nagaoka, T. Jamneala, M. Grobis, M. F. Crommie, Temperature dependence of a single kondo impurity. *Phys. Rev. Lett.* **88**, 077205 (2002).
34. Y. Luh, Bound state in superconductors with paramagnetic impurities. *Acta Phys. Sin.* **21**, 75 (1965).
35. A. I. Rusinov, Superconductivity near a Paramagnetic Impurity. *J. Exp. Theor. Phys. Lett.* **9**, 85 (1969).
36. H. Shiba, Classical Spins in Superconductors. *Prog. Theor. Phys.* **40**, 435–451 (1968).
37. T. Matsuura, The effects of impurities on superconductors with kondo effect. *Prog. Theor. Phys.* **57**, 1823–1835 (1977).
38. W. Krenner, D. Kühne, F. Klappenberger, J. V. Barth, Assessment of scanning tunneling spectroscopy modes inspecting electron confinement in surface-confined supramolecular networks. *Sci. Rep.* **3**, 1454 (2013).
39. G. Reecht, B. W. Heinrich, H. Bulou, F. Scheurer, L. Limot, G. Schull, Imaging isodensity contours of molecular states with STM. *New J. Phys.* **19**, 113033 (2017).
40. L. Nguyen, H.-P. Komsa, E. Khestanova, R. J. Kashtiban, J. J. P. Peters, S. Lawlor, A. M. Sanchez, J. Sloan, R. V. Gorbachev, I. V. Grigorieva, A. V. Krasheninnikov, S. J. Haigh, Atomic defects and doping of monolayer $NbSe_2$. *ACS Nano* **11**, 2894–2904 (2017).
41. F. Bischoff, W. Auwärter, J. V. Barth, A. Schiffrin, M. Fuhrer, B. Weber, Nanoscale phase engineering of niobium diselenide. *Chem. Mater.* **29**, 9907–9914 (2017).
42. H. v. Löhneysen, A. Rosch, M. Vojta, P. Wölfle, Fermi-liquid instabilities at magnetic quantum phase transitions. *Rev. Mod. Phys.* **79**, 1015–1075 (2007).
43. K. J. Franke, G. Schulze, J. I. Pascual, Competition of superconducting phenomena and kondo screening at the nanoscale. *Science* **332**, 940–944 (2011).
44. H. Huang, C. Padurariu, J. Senkpiel, R. Drost, A. L. Yeyati, J. C. Cuevas, B. Kubala, J. Ankerhold, K. Kern, C. R. Ast, Tunnelling dynamics between superconducting bound states at the atomic limit. *Nat. Phys.* **16**, 1227–1231 (2020).
45. D. Chatzopoulos, D. Cho, K. M. Bastiaans, G. O. Steffensen, D. Bouwmeester, A. Akbari, G. Gu, J. Paaske, B. M. Andersen, M. P. Allan, Spatially dispersing Yu-Shiba-Rusinov states in the unconventional superconductor $FeTe_{0.55}Se_{0.45}$. *Nat. Commun.* **12**, 298 (2021).
46. A. V. Balatsky, I. Vekhter, J.-X. Zhu, Impurity-induced states in conventional and unconventional superconductors. *Rev. Mod. Phys.* **78**, 373–433 (2006).
47. B. W. Heinrich, J. I. Pascual, K. J. Franke, Single magnetic adsorbates on s-wave superconductors. *Prog. Surf. Sci.* **93**, 1–19 (2018).
48. E. W. Hudson, K. M. Lang, V. Madhavan, S. H. Pan, H. Eisaki, S. Uchida, J. C. Davis, Interplay of magnetism and high-T_c superconductivity at individual Ni impurity atoms in $Bi_2Sr_2CaCu_2O_{8+\delta}$. *Nature* **411**, 920–924 (2001).
49. S. Lu, H. Nam, P. Xiao, M. Liu, Y. Guo, Y. Bai, Z. Cheng, J. Deng, Y. Li, H. Zhou, G. Henkelman, G. A. Fiete, H.-J. Gao, A. H. MacDonald, C. Zhang, C.-K. Shih, PTCDA molecular monolayer on Pb thin films: An unusual π-electron Kondo system and its interplay with quantum-confined superconductor. arXiv:2102.11471 [cond-mat. supr-con] (23 February 2021).
50. M. I. Salkola, A. V. Balatsky, J. R. Schrieffer, Spectral properties of quasiparticle excitations induced by magnetic moments in superconductors. *Phys. Rev. B* **55**, 12648–12661 (1997).
51. P. Giannozzi, S. Baroni, N. Bonini, M. Calandra, R. Car, C. Cavazzoni, D. Ceresoli, G. L. Chiarotti, M. Cococcioni, I. Dabo, A. D. Corso, S. de Gironcoli, S. Fabris, G. Fratesi, R. Gebauer, U. Gerstmann, C. Gougoussis, A. Kokalj, M. Lazzeri, L. Martin-Samos, N. Marzari, F. Mauri, R. Mazzarello, S. Paolini, A. Pasquarello, L. Paulatto, C. Sbraccia, S. Scandolo, G. Sclauzero, A. P. Seitsonen, A. Smogunov, P. Umari, R. M. Wentzcovitch, QUANTUM ESPRESSO: A modular and open-source software project for quantum simulations of materials. *J. Phys. Condens. Matter* **21**, 395502 (2009).
52. J. P. Perdew, K. Burke, Y. Wang, Generalized gradient approximation for the exchange-correlation hole of a many-electron system. *Phys. Rev. B* **54**, 16533–16539 (1996).
53. M. J. van Setten, M. Giantomassi, E. Bousquet, M. J. Verstraete, D. R. Hamann, X. Gonze, G. M. Rignanese, The PseudoDojo: Training and grading a 85 element optimized norm-conserving pseudopotential table. *Comput. Phys. Commun.* **226**, 39–54 (2018).
54. M. Cococcioni, S. de Gironcoli, Linear response approach to the calculation of the effective interaction parameters in the LDA + U method. *Phys. Rev. B* **71**, 035105 (2005).
55. W. Li, X. Qian, J. Li, Phase transitions in 2D materials. *Nat. Rev.Mater.* **6**, 829–846 (2021).
56. N. Hatter, B. W. Heinrich, M. Ruby, J. I. Pascual, K. J. Franke, Magnetic anisotropy in Shiba bound states across a quantum phase transition. *Nat. Commun.* **6**, 8988 (2015).

Acknowledgments: We are grateful to D. Xiao and M. Xie for helpful discussions. **Funding:** This work was primarily supported by the National Science Foundation (NSF) through the Center for Dynamics and Control of Materials: an NSF MRSEC under cooperative agreement no. DMR-1720595. J.L. and F.G. were supported by the Robert A. Welch Foundation under award number F-1990-20190330. Other supports were from NSF grant nos. DMR-1808751 and DMR-1949701, the Welch Foundation F-1672, F-1814, and the National Natural Science Foundation of China (grant nos. 11774268 and 11974012). **Author contributions:** M.L. and C.-K.S. designed and coordinated the experiments. M.L. and S.L. carried out the STM/STS measurements. M.L., J.Y., and H.K. performed the sample growth. C.T. and Y.S. participated in the preparation of 1T-$NbSe_2$/2H-$NbSe_2$ vertical heterostructures. J.L. performed the DFT calculations. M.L., S.L., C.Z., and C.-K.S. analyzed the STM/STS data. J.L. and F.G. performed the theoretical analysis. K.L. and C.-K.S. co-supervised the MBE growth. M.L., F.G., and C.-K.S. wrote the paper with input from all authors. All authors contributed to the scientific discussion. **Competing interests:** The authors declare that they have no competing interests. **Data and materials availability:** All data needed to evaluate the conclusions in the paper are present in the paper and/or the Supplementary Materials.

Submitted 22 March 2021
Accepted 30 September 2021
Published 19 November 2021
10.1126/sciadv.abi6339